



Interferences between natural and anthropic hazards in marine-coastal environments: Assessing transport from land to the offshore systems in the Crotone basin (Ionian Sea)

Elvira Oliveri^{a,*}, Antonella Ausili^b, Mattia Barsanti^c, Fabio Conte^c, Ivana Delbono^c, Marianna Del Core^d, Luigi Giaramita^d, Salvatore Passaro^e, Francesco Placenti^d, Enza Maria Quinci^d, Elena Romano^b, Nadia Sabatino^a, Antonio Schirone^c, Giorgio Tranchida^d, Mario Sprovieri^d

^a Institute of Anthropic Impacts and Sustainability in the Marine Environment (IAS), National Research Council (CNR), Lungomare Cristoforo Colombo, 4521, 90149, Loc. Addaura, Palermo, Italy

^b ISPRA, Institute for Environmental Protection and Research - National Centre for Environmental Characterization and Protection of the Marine Coastal Areas, Via V. Brancati 60, Rome, Italy

^c ENEA Italian National Agency for New Technologies, Energy and Sustainable Economic Development, Marine Environment Research Centre S. Teresa, 19032, Pozzuolo di Lerici, La Spezia, Italy

^d Institute of Anthropic Impacts and Sustainability in the Marine Environment (IAS), National Research Council (CNR), Via Del Mare 3, 91021, Torretta Granitola, (TP), Italy

^e Institute of Marine Science (ISMAR), National Research Council (CNR), Calata Porto di Massa, 80133, Napoli, (NA), Italy

ARTICLE INFO

Keywords:

Natural hazards
Flood events
Marine coastal sediments
Pollution
Heavy metals
²¹⁰Pb sediment dating

ABSTRACT

This paper is focused on the field-evidence of environmental hazard associated with flood events in highly contaminated marine coastal areas. The Crotone site (Ionian Sea), in the 1900s hosted a large industrial settlement (with the largest plant in Europe of zinc production, phosphorus manufacture, etc.) which left a severe legacy of environmental pollution. Here, we report the results of an investigation related to the distribution of heavy metals (Zn, Pb, Cd, Cu) in 230 sediment cores that allowed a detailed reconstruction of the contamination due to the discharge at sea of industrial wastes deriving from the Zn-sulphides leaching processes. High concentrations of heavy metals (e.g., Zn > 5000 mg kg⁻¹) accumulated in sediments of the seabed along coastline, exposed to the fluvial and coastal dynamics, act as a potential long-term source of pollution for the marine ecosystem. Fingerprints of historically flash flood events evidenced in two ²¹⁰Pb dated sediment cores suggest that these catastrophic events played a crucial role in the land-to-sea transferring (and sequent dispersing effects) of highly polluted sediments. Anomalous depositions of heavy metals-rich sediments in the offshore system (4–6 km from the coastline) testify secondary contamination due to mobilization and redistribution of old contaminated sediment due to flood events. These interactions between natural and anthropic hazards trigger cumulative mechanisms of multiple-pollution and transfer of contamination from polluted nearshore to offshore nearly pristine areas through main canyon axes.

1. Introduction

The exponential growth of the world economy over the last 70 years exposed coastal areas to significant pressures, as combined effects of increase of urbanization and development of infrastructure and industrial plants, such as refineries and chemical and steel factories. Several Mediterranean coastal areas currently witness the legacy of this

economic growth with large volumes of wastes deposited in extensive landfills and near-shore dumps. Most of the contaminants derived from these industrial activities affect the aquatic environment, its ecosystem and the marine sediments which represent the final sink and a potential secondary source of highly toxic, generally persistent, and bio-accumulative pollutants (Kowalewska et al., 2011; Bonsignore et al., 2013; Salvaggio Manta et al., 2016; Ausili et al., 2020). The conventional

* Corresponding author.

E-mail address: elvira.oliveri@cnr.it (E. Oliveri).

<https://doi.org/10.1016/j.ecss.2022.107854>

Received 17 June 2021; Received in revised form 23 March 2022; Accepted 8 April 2022

Available online 15 April 2022

0272-7714/© 2022 Elsevier Ltd. All rights reserved.

approach to assess environmental pollution is mainly focused on detailed analyses of contaminants in sediments, seawater and biota from specific contexts (e.g., Borch et al., 2010), without considering combined effects potentially triggered by geomorphological/geological components (presence of river mouths, highly variable hydrological regimes, instability of slopes and lands, high runoff capacity, etc.) that could be strictly associated to natural risks (earthquakes, floods, landslides, tsunamis, etc.) and potentially produce multi-hazard effects and amplified hazard chains (e.g., Massarra et al., 2019). For instance, the supply of sediments by rivers represents a primary pathway of pollutants from land to the sea (e.g., Viers et al., 2009). This could be significantly amplified during flash flood events with an exponential effect of surface soils mobilization and transfer in the marine environment (Ollivon et al., 1999; Velasco et al., 2006; Sicre et al., 2008; Martínez-Santos et al., 2015; Irabien et al., 2019). In the Mediterranean region, flash floods represent an important contribution to particulate inputs to the sea, although only a few studies have explored mechanisms of mass transfer and dispersion of contaminants from land to the sea under these conditions (Marín-Guirao et al., 2007; Bradley et al., 2010; Roussiez et al., 2011; The MerMex Group, 2011; Oursel et al., 2014).

This research deals with the case study of the Crotona marine coastal area (Southern Italy, Ionian Sea) where the interferences between environmental contamination and high-energy floods were accurately documented, thus offering a good example of multi-hazard impact. A multi-proxy sedimentary investigation, including sedimentological, mineralogical, geochemical (heavy metals) and isotopic (^{210}Pb , ^{137}Cs , ^{40}K , ^{226}Ra) tools, has been achieved to reconstruct the contamination status of the Crotona coastal area and to examine the extension of the marine pollution as consequence of remobilization and dispersion of highly contaminated sediment caused by flood events. The results highlight a systematic amplification of the environmental damage caused by remobilization and relocation of polluted sediments in offshore distal areas. Flood events will likely increase in the upcoming decades due to global climate change (Alfieri et al., 2017; Arnell and Gosling, 2016) and the damage caused by floods may increase up to 20-fold by the end of the century especially along coastal areas (Wimsemius et al., 2016). Consequently, polluted marine sediments could be transported, by intensive flooding events, in highly delicate marine environments and negatively affect wildlife and biodiversity in the deep

sea system.

2. Study area

The study area represents the easternmost emergent sector of the Calabrian arc, which belongs to the Calabrian subduction system and is related to the opening of the Tyrrhenian Sea Basin. Crotona is located on the Ionian Sea (Calabrian Region, Italy; Fig. 1A) and is part of the homologous Basin, which represents the upper Neogene-Quaternary fore-arc basin of the Ionian arc-trench system, generated by eastward rollback of a west-dipping subduction zone associated with extension in the Tyrrhenian back arc basin (Bonardi et al., 2001; Zecchin et al., 2004; Massari et al., 2010). Due to its tectonic activity (Zecchin et al., 2020), this area is characterized by long-term uplift (Ferranti et al., 2009) testified by the exposure of flight of marine terraces (Zecchin et al., 2004) and by the emerging submarine canyon head (Zecchin and Caffau, 2020). This resulted in a generalized over steepening that triggers a diffuse slope instability ranging from small (Confuorto et al., 2015) to large scale effects ("mega landslide"; Zecchin et al., 2018). The geological facies are progressively younger eastward in the study area (from the Sila Massif to the Holocene fluvial basins; Fig. 1B) with a dominating left-lateral striking system that constraints the tectonic evolution of the area (Fig. 1B), while the whole easternmost sector shows a prevailing eastward oriented reticulate stream (Fig. 1C). The Crotona Basin is a depocenter essentially filled by.

Serravallian to Pleistocene deep marine pelitic sediments and by arenaceous-conglomerate also arising from marine terraces (Roda, 1964; Fig. 1B). The Neto and Esaro (Fig. 1A–C) are the most important rivers in the area, feeding the Deep Ionian Basin through the Neto-Lipuda and Esaro submarine Canyons (Rebesco et al., 2009; Fig. 1A). Furthermore, among the river streams the Passovecchio Stream can be periodically characterized by relevant discharges specially during alluvial events (Fig. 1D). The lithogenic supply of the Neto River is mainly constituted by quartz-feldspar sands because the upper drainage system flows on the plutonic (granite) and metamorphic (gneiss) rocks of the Sila Massif, locally covered by thick weathering profiles (Messina et al., 1991; Le Pera et al., 2001; Fig. 1B). The Esaro drainage system involves only the Plio-Quaternary sediments of the Crotona Basin where lithogenic supply contains mainly silicoclastic and carbonate fraction (Roda,

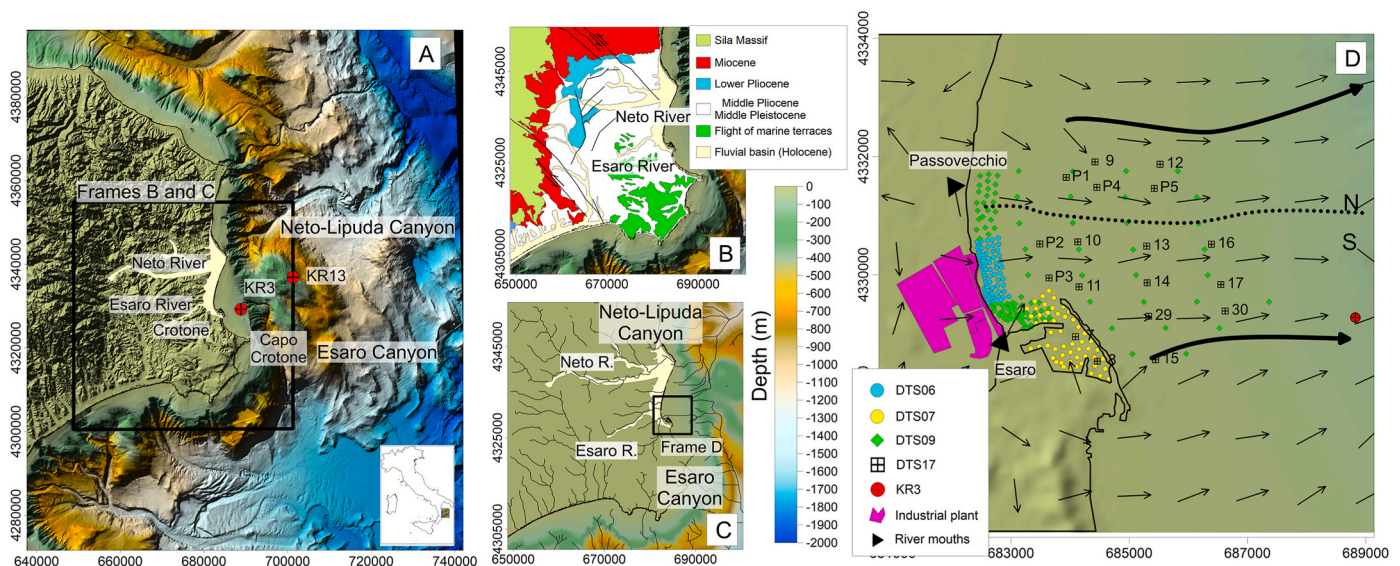


Fig. 1. Location map of the study area. A) Digital Terrain Model and location of the main river basins (Neto, Esaro), canyons (Neto-Lipuda and Esaro) and of the KR3 and KR13 sediment cores; B) Geology of the Crotona promontory (modified after Zecchin et al., 2020); C) Reconstructed streamlines of the Neto and Esaro Rivers and of the Neto-Lipuda and Esaro Canyons; D) Location map of the sampling stations used for geochemical characterization of the area. Dotted line divides the offshore in the northern sector (N) and the southern sector (S). Vectors report reconstructed slope directions. The two bold arrows indicate the main directions of Neto-Lipuda and Esaro Canyons.

1964; Zecchin et al., 2012, 2020; Fig. 1B). Morphological features of the bottom sediments were reconstructed by Digital Terrain Model (DTM; Fig. 1) derived by joining topographic and multibeam data (EMODnet data-centre, Fig. 1). The main DTM frame shows ca. 260 km² at 50 m grid cell size (Fig. 1A), ranging from 1870 m to 2000m of depth. The Esaro and Neto Rivers and the easternmost marine canyons linked to the Crotone Cape (i.e., Esaro and Neto-Lipuda; Rebesco et al., 2009) have been also indicated (Fig. 1A).

An intensive metallurgical activity of zinc purification by applying roast-leach-electro-win technique from Zn-sulphide compounds (Monhemius, 1980), was active in the Crotone area between the 1930s and the 1990s. Huge amounts of tailings, mainly containing ferrites of zinc, lead, cadmium and copper (deposited on land and discharged at sea) represent a critical legacy of this industrial activity. An additional chemical plant of phosphorous production generated important radioactive wastes (e.g., phosphogypsum, Ca-metasilicates) containing Naturally Occurring Radioactive Materials (NORM) (IAEA 599, 2013). Furthermore, since 1996, a new chemical factory dedicated to production of zeolite detergents was added to the industrial compartment of Crotone. In the '90s all the industrial activities (except for that connected to zeolite detergents) were definitively closed.

This industrial complex is placed near to the mouth of the Esaro River which, along with the Passovecchio stream, has seen several events of flash floods and overflowing causing destructive impacts on land often with casualties. Major effects have been reported for several historical flood events in 1954, 1957, 1959, 1976 and 1996 (Petrucchi et al., 1996, 2012; Petrucchi and Dodaro, 1998; Mendicino, 2006; Canale et al., 2020). In particular, the most recent flash flood in 1996 has been reported as highly destructive and caused relevant damages to several compartments of the industrial plant and the near town (Macchione et al., 2019; Costabile et al., 2020).

3. Materials and methods

3.1. Sampling

Four sediment sampling surveys (Fig. 1D) were carried out in the study area: i) in 2006 (DTS06) in the marine area in front of the industrial plant; ii) in 2007 (DTS07), within the Crotone harbor area; iii) in 2009 (DTS09), in the sectors facing the Esaro and Passovecchio river mouths and offshore within ~4 km from the coast; iv) in 2017 (DTS17), in the offshore within ~4 km from the coast (Fig. 1D), but also at distance from the coast of ~6 km (depth of 70 m) at the head of the Esaro canyon system (KR3 sediment core, Fig. 1A and 1D) and at a distance from the coast of ~19 km (depth of 369 m, KR13, sediment core; Fig. 1A).

The sediment cores collected in 2006 (DTS06) and 2009 (DTS09) were sampled by the 'Delegate Commissioner for Environmental Emergency in the Calabria Region' and by the Regional administration, respectively; the 2007 cores (DTS07) were collected by the 'Reggio Calabria Civil Engineering Maritime Works'. All the sampling activities (in 2006, 2007 and 2009) used a vibrocorer with internal liner, to avoid cross contamination and collected a total of 73, 54 and 103 sediment cores, respectively. The sediment cores from the harbor area (DTS07) were sub-sampled at levels of 0–20 cm, 30–50 cm, 100–120 cm and 180–200 cm, for a total of 186 samples. The sediment cores from the coastal and offshore areas (DTS06 and DTS09) were sub-sampled at 0–10 cm, 10–30 cm, 30–50 cm, 100–120 cm and 180–200, for a total of 230 and 462 samples, respectively.

The 2017 sediment cores (DTS17) were collected by the Institute of Anthropic impacts and Sustainability in the marine environment of the Italian Research Council (IAS-CNR) using a 60 cm cylindric box-core sampler. They consisted in i) 18 cores ranging in length between 6 and 38 cm, sliced at 1–2 cm intervals and for a total of 205 samples and ii) two longer cores KR3 (35-cm long) and KR13 (42-cm long) sliced at 1 cm intervals for a total of 76 samples.

3.2. Grain size analysis

Grain size measurements were carried out in all the collected cores (DTS06, DTS07, DTS09 DTS17) to characterize main sedimentary processes in the study area. All samples were treated with a solution of hydrogen peroxide (30 w/v – 100 vol%) and distilled water (1:4) for 24/48 h to remove organic matter, then washed for eliminating salts. Grain size for DTS06, DTS07 and DTS09 was previously wet-separated into coarser and fine fractions; then analyzed by ASTM series sieves (>63 µm) and X-ray sedigraph (<63 µm). Grain size analyses for the DTS17 samples were carried out using a Horiba Partica LA-950V2 laser granulometer.

3.3. Mineralogical and SEM analysis

Bulk sample mineralogy was performed on selected samples of DTS17, as representative of the coastal and offshore sector, in order to assess the main sources of sediments in the study area. Dried (T = 50 °C) and powdered samples were analyzed by X-ray diffraction (XRD) using a D8 Discover Bruker, equipped with a Sol-X detector, Cu-Kα radiation and a scanning speed of 2 2°/min. The semi-quantitative analysis of minerals was performed according to the methods and data reported in Schultz (1964) and Barahona et al. (1982). For SEM observation, the untreated aliquot of sediment was mounted on aluminum stubs, sputter coated with gold and observed under a Scanning Electron Microscope (SEM) EVO MA 10 ZEISS equipped with an EDS Bruker Quantax 200 detector.

3.4. Heavy metals analysis

The analysis was performed on all the cores (DTS06, DTS07, DTS09 DTS17). Heavy metals analysis on samples of DTS06, DTS07 and DTS09 was carried out by previous microwave-assisted digestion with a mixture of concentrated hydrochloric and nitric acids (EPA 3050, EPA 3051A). They were then measured according to different EPA methods (EPA 6020, EPA 200.8) which involved Inductively Coupled Plasma Mass Spectrometry (ICP-MS) or atomic emission spectrometry (ICP-AES). Heavy metals were analyzed on the < 2 mm fraction and no normalization to different grain size fractions was adopted.

Sediment samples of the DTS17 were dried at 35 °C, ground and homogenized in an agate mortar to a fine powder. For metal determinations, ~0.20 g of dry sediment was digested with an acid mixture: nitric acid (67% w/v), hydrochloric acid (37% w/v), hydrofluoric acid (40% w/v) and boric acid in a ratio of 3:1:1:5. The acid mixture and sample were introduced into a closed teflon vessel (EPA 3052 and EPA 6010D methods) and subjected to digestion using a DISCOVER SP-D80 microwave oven (CEM Corporation). Sample solution and reagents blank for total TM, were analyzed by Inductively Coupled Plasma-Optical Emission Spectrometer (iCAP 6000, Thermo Scientific; US EPA, 2014).

The accuracy estimated to be ~94–106% and the precision (routinely better than 7%; RDS%, n = 3) of the analytical procedures have been checked by applying to the Reference Standard Material (PACS-2, Marine Sediment Reference Materials for Trace Metals and other Constituents- NRC-CNRC). Finally, duplicate samples (about 20% of the total samples) were analyzed to estimate the reproducibility (better than 94%). Finally, results are reported as mg kg⁻¹ dry weight (T = 105 °C).

3.5. Radiometric analysis

Radiometric analysis were carried out only in samples from DTS17 to quantify Naturally Occurring Radioactive Materials (NORM) in surficial sediments and establish the geochronology in the KR3 and KR13 sedimentary cores. Radiometric analyses were performed by gamma spectrometry at ENEA Marine Environment Research Centre. Each sample

was counted for 2–3 days on high-purity germanium detectors, with carbon fiber window for low energy gamma ray's detection. The detectors have an efficiency of 60% and a resolution of 2.2 keV at the 1.33 MeV ^{60}Co gamma emission. The calibrations for ^{238}U series radionuclides, ^{40}K and ^{137}Cs were performed using CANMET (CANada centre for Mineral and Energy Technology) reference standard DL1a, IAEA reference standard RG K-1 and multi-elemental Eckert & Ziegler Analytics reference standard QCYA48, respectively. Quality controls are routinely realized by analyzing standard reference materials of the International Atomic Energy Agency (IAEA-385). Detector blanks are monthly determined from measurements performed on empty sample containers over a few days. Detection limits were calculated according to Currie (1968), considering a “well-known” blank: where measurements are indicated as 0, the detection limit is reported instead of uncertainty. Sample self-absorption of the low-energy ^{210}Pb gamma (47 keV) by the calibration standard and sample is made using the method of Cutshall et al. (1983). ^{226}Ra is determined by averaging the calculated activities from daughters ^{214}Bi and ^{214}Pb . ^{226}Ra and ^{40}K have long half-lives, hence are considered constant. ^{210}Pb dating method has been widely used for establishing geochronology in marine sediments on time scales of ~110 years, compatible with ^{210}Pb physical half-life. This method is based on the decay of the unsupported $^{210}\text{Pb}_{\text{ex}}$ fraction (equal to the total ^{210}Pb concentration minus the concentration of ^{226}Ra) inside the sediment, and it must always be verified using an independent time marker (Smith, 2001). For this purpose, a radionuclide frequently used is the ^{137}Cs , an artificial radionuclide that has been introduced in the environment mainly during the nuclear bomb testing in atmosphere and had its maximum release just before the *Treaty Banning Nuclear Weapon Tests in the Atmosphere, in Outer Space, and Under Water* (1963). Among the typically used dating models based on $^{210}\text{Pb}_{\text{ex}}$ profiles, the Constant Flux - Constant Sedimentation (CFCs) dating model (Sanchez-Cabeza and Ruiz-Fernández, 2012; Krishnaswamy et al., 1971; Appleby and Oldfield, 1983) was applied on KR3 sediment core, assuming a constant flux of $^{210}\text{Pb}_{\text{ex}}$ at the sediment-water interface and a constant Mass Accumulation Rate (MAR, $\text{g cm}^{-2} \text{y}^{-1}$). Since this model is based on $^{210}\text{Pb}_{\text{ex}}$ concentration, data have been normalized to pelitic (silt + clay) fraction before fitting. The ^{137}Cs specific activities have been normalized to the same fraction to identify the layer corresponding to 1963. On KR13 sediment core the Constant Rate of Supply (CRS) model was applied (Appleby and Oldfield, 1978; Robbins, 1978), since the $^{210}\text{Pb}_{\text{ex}}$ trend suggests that the MAR is not constant. Since this method uses the inventory of $^{210}\text{Pb}_{\text{ex}}$ under a given layer to determine its age, no age can be assigned to layers deeper than the “equilibrium depth”, where $^{210}\text{Pb}_{\text{ex}}$ reaches the zero value. Dating models have been applied using the mass depth scale (g cm^{-2}) to compensate possible effects of sediment core compaction.

3.6. Statistical analysis

Distribution maps were generated for heavy metals based on a vector layer core locations to synthesize the main information from the huge available datasets. The heavy metals concentrations were interpolated in QGIS 3.14.16 using RST (Regularized Spline with Tension) method, described by Mitášová and Mitáš (1993). The interpolation reports a buffer area with a fixed distance of 1 km from sampling sites.

4. Results

4.1. Grain size and mineralogy

The grain size distribution of the analyzed samples is reported in the Shepard diagram (Fig. 2A). The sediments along the coastal sector and in the northern offshore sector (DTS06, DTS09, DTS17; Fig. 1D) are mainly characterized by sands (average value 80%; yellow ellipse in Fig. 2A). The sediments in the outer sector of the harbor, close to the mouth of the Esaro River, and in the southern offshore sector (DTS07, DTS09, DTS17; Fig. 1D) principally consist of silty sands and sandy silt (red ellipse in Fig. 2A), except for some cases where clayey-silt grain size occurs. In the southern offshore sector, some DTS17 cores (16, 17, 29, 30) show yellow sands (95–100%) with unconsolidated facets and lack of silt and clay in the topmost levels (Fig. S1) in contact with the underlying silty sediments (Fig. S2).

The harbor area (DTS07, DTS17; Fig. 1D) is mainly characterized by silt-clayey sediments that change to sandy or sandy-silt with depth (blue ellipse in Fig. 2A). Thus, an evident sedimentological dissimilarity emerges between the northern sector, characterized by prevalent sandy sediments, and the southern sector with silty and clayey deposits (Fig. 2A). This primarily suggests a predominant contribution of terrigenous supply from the Esaro River (Fig. 1D).

The mineralogical features (Figs. 2B and 2C) of the dark to grey sands in the northern offshore sector mainly consist of quartz (21–35%; mean 26%), K-feldspar (17–30%; mean 27%), albite (18–45%; mean 29%) and, secondarily, muscovite (13–23%) and calcite (2–5%, mean 4%). The silty sands in the southern sector shows similar mineralogical composition even if the K-feldspar (2–40%; mean 13%) and albite (3–17%; mean 9%) decrease whereas percentages of calcite increase (4–13%; mean 10%); also clay minerals are present (8–48%; mean 12%). Calcite (15–21%; mean 17%) and clay minerals (28–36%; mean 30%) together with quartz (19–24%; mean 20%) become primary constituents in the clayey silt sediments, while the feldspars are absent or only accessory minerals (<5%). K-feldspar (mean 64%) and quartz (mean 19%) dominate the mineralogical composition of the topmost yellow sandy layers with minor percentages of albite (mean 8%) and calcite (<3%).

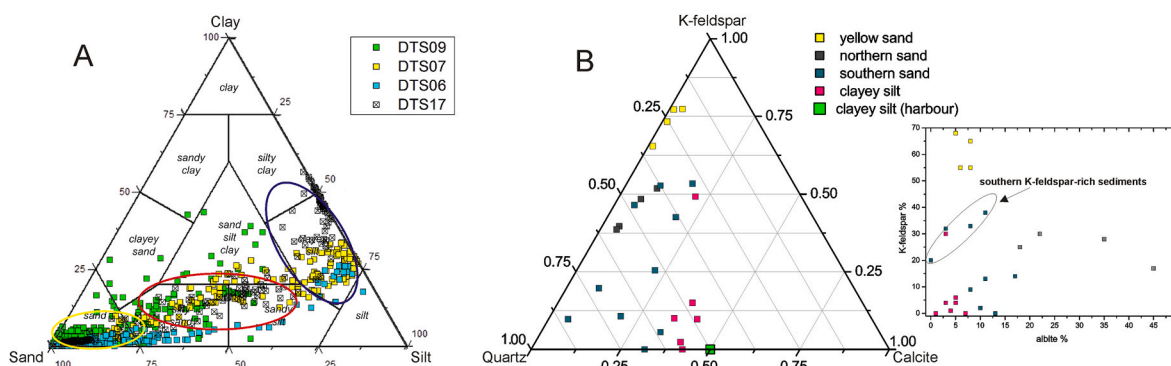


Fig. 2. A) Grain size of DTS06, DTS07, DTS09 and DTS17 sediments in the Shepard's diagram (1958). Blue ellipse includes samples from the harbor area; Red ellipse includes samples from the area in front of the Esaro River and southern offshore sector; yellow ellipse includes samples from the northern coastal and offshore sectors. B) Mineral ternary plots. C) K-feldspar-albite diagram includes southern sediments characterized by low albite percentages. (For interpretation of the references to color in this figure legend, the reader is referred to the Web version of this article.)

The SEM-EDS analyses of some yellow sand samples revealed the presence of Ca-rich silicates with limited percentages of Mg and Fe (Fig. S3). Particularly, measured values of $\text{Si}/\text{Al} > 3$ and $\text{Ca}/\text{Si} > 1$ document a synthetic origin for feldspars ($\text{Si}/\text{Al} = 1\text{--}3$, $\text{Ca}/\text{Si} < 0.6$ for natural feldspar, according to Yang et al., 2014 and Liu et al., 2019). These Ca-silicates could belong to the zeolite series, reasonably artificial in origin, due to the high Ca contents and the presence of traces of Fe and Mg (Villa et al., 2010).

4.2. Heavy metals

4.2.1. Spatial distribution in coastal and offshore sectors

The heavy metal concentrations (Cd, Cu, Pb, Zn) are reported in Table S4 and their distributions, at the different depths, are shown in the box-whiskers plots (Fig. S5). Normalization to Al was not applied as this element was an essential component of treatment processes of bauxite. The distribution map of Al shows, in the harbor area, a highly inhomogeneous pattern for the entire investigated sedimentary column thus supporting the hypothesis of a pervasive industrial contamination of this element (Fig. S6). Also, the approach to normalizing heavy metals concentration to grain size appears inappropriate due to the presence of nearly 100% sands in most samples, except for several sediments in the harbor area.

The concentrations of heavy metals widely vary between 0.005 and 82.40 mg kg^{-1} for Cd, 0.05 and 297.50 mg kg^{-1} for Cu, 0.40 and 2659.20 mg kg^{-1} for Pb, 2.80 and 22027.79 mg kg^{-1} for Zn (Table S4). In Fig. 3 we reported the spatial distribution of Zn in the different sedimentary levels. The maps clearly show how the highest concentrations ($>5,000 \text{ mg kg}^{-1}$) characterize the internal harbor area and the coastal sector, in front of the mouth of the Esaro River, and identify sectors of major impact at sea (hereafter named 'impact area'). The external area, which represents the rest of the investigated zone, shows significantly lower concentrations ($<200 \text{ mg kg}^{-1}$), except for samples S105, S109, and S112 (30–50 cm) located in proximity of the outer dam of the harbor (Fig. 3b).

The correlation matrix shows a strong covariance among Zn, Pb, Cd, and Cu ($0.6 < r < 0.8$; p value < 0.05) reasonably suggesting analogue contamination pathways and sources (mainly related to the working processes on sphalerite minerals) reflecting leaching of source minerals. In the impact area, the heavy metals concentrations show a general decreasing trend along depth, with some exceptions documenting high values also in deeper levels (Fig. S5).

4.2.2. Vertical distribution of heavy metals in the offshore DTS17 cores

Most of the analyzed heavy metals show lower values in the cores of the northern sector than in those of the southern one (Fig. 4). In addition, also in 3 cores (29, 17, 16) values of the same order of magnitude of those found in the "impact area" are detected; the core 29 shows Zn values with averages of 400 mg kg^{-1} in the interval 9–18 cm (Fig. 4) followed by a weak decreasing trend (172–335 mg kg^{-1}) in the interval 5–8 cm (Fig. 4). In the topmost sediments, where the yellow sands are present (Fig. S2), Zn significantly drops to values comprised between 20 and 31 mg kg^{-1} . The Pb concentration patterns appear reasonably like those of Zn with average values of 100 mg kg^{-1} in the interval 9–18 cm followed by a sharp decrease in the upper sediments (Fig. 4).

The patterns of Cd and Cu are well correlated to other metals and show the highest values at depth of 10 cm below the top (up to 3 and 34 mg kg^{-1} , respectively). In the core 17 the Zn and Pb concentrations reach very high values (up to 1,374 and 366 mg kg^{-1} , respectively) in the interval 14–22 cm (Fig. 4). Similarly, Cd and Cu concentrations increase in the deepest sedimentary levels where reach values up to 9 and 49 mg kg^{-1} respectively (Fig. 4). All the heavy metals strongly decrease in the topmost sediments, where yellow sands deposited (Fig. 4). In the core 16, at the deepest levels 10–25 cm, the Zn and Pb concentrations result to be elevated (up to 740 and 250 mg kg^{-1} , respectively). Following the same scheme of the two previous cores, a sharp decrease

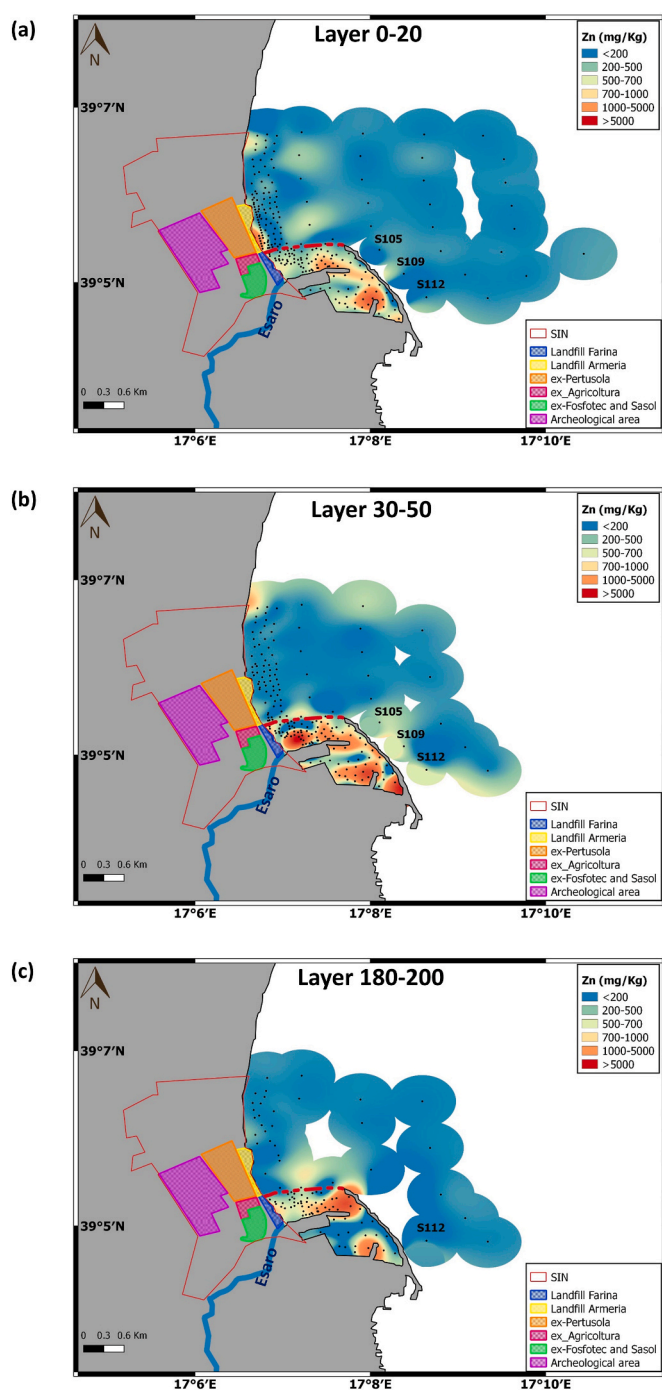


Fig. 3. Distribution maps of Zn in the DTS06, DTS07, DTS09 sediments at 0–20 cm, 30–50 cm, 180–200 cm depths. The red dot line delimits the 'impact zone'. (For interpretation of the references to color in this figure legend, the reader is referred to the Web version of this article.)

in heavy metals concentration is evident in the topmost sediments constituted by yellow sands (Fig. 4).

4.3. Timing of contamination in the offshore cores KR3 and KR13

4.3.1. Age model

In the KR3 sediment core, depth-age was determined using the CFCs (Constant Flux - Constant Sedimentation) dating model, fitting the $^{210}\text{Pb}_{\text{ex}}$ data linearly, with variable uncertainties. The $^{210}\text{Pb}_{\text{ex}}$ dating has been confirmed by the ^{137}Cs trend, since the knee near the bottom of

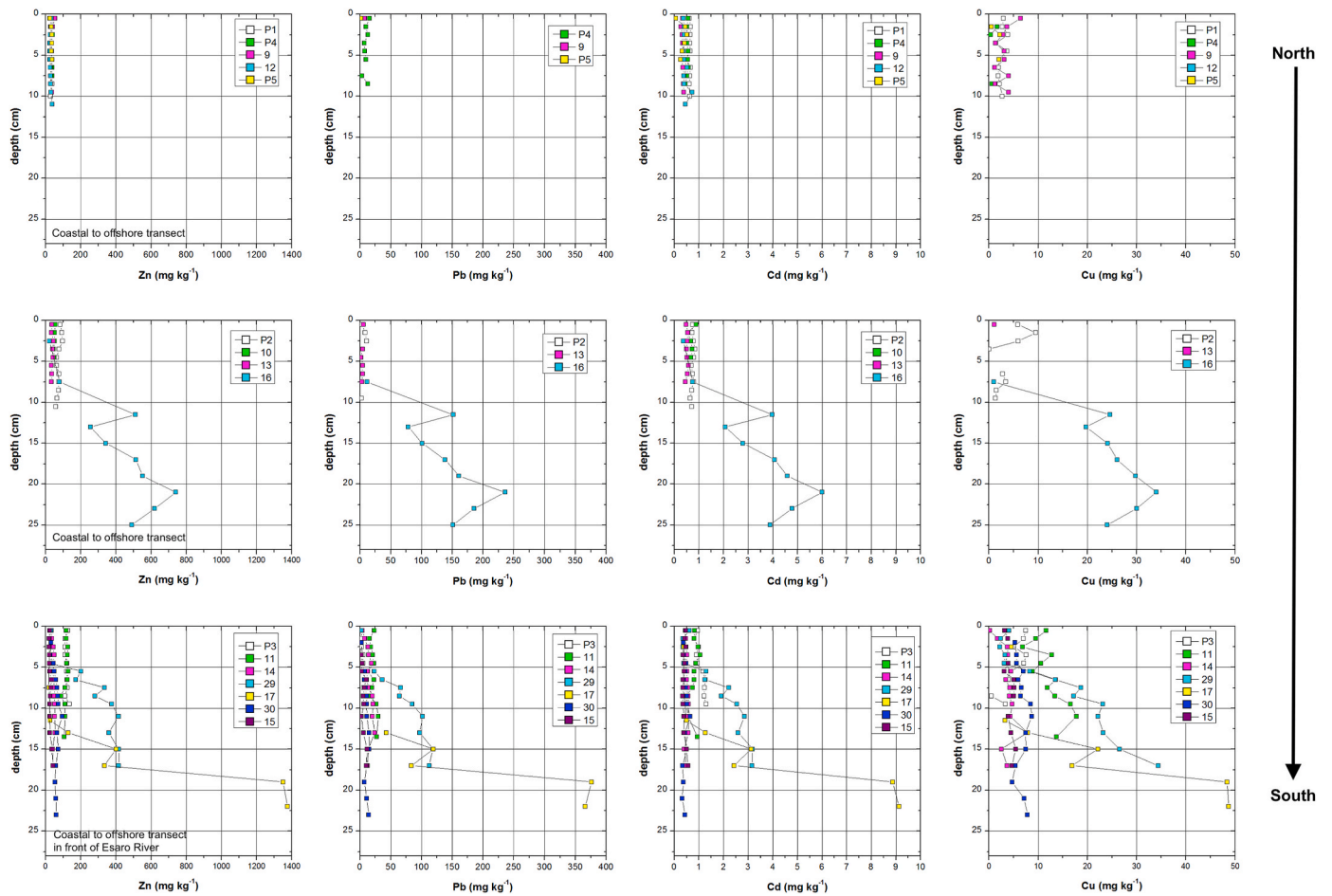


Fig. 4. Depth profiles of Cd, Cu, Pb, Zn in the DTS17 cores (northern and southern sectors). Core 29, 16, 17 present yellow sands in the topmost levels. (For interpretation of the references to color in this figure legend, the reader is referred to the Web version of this article.)

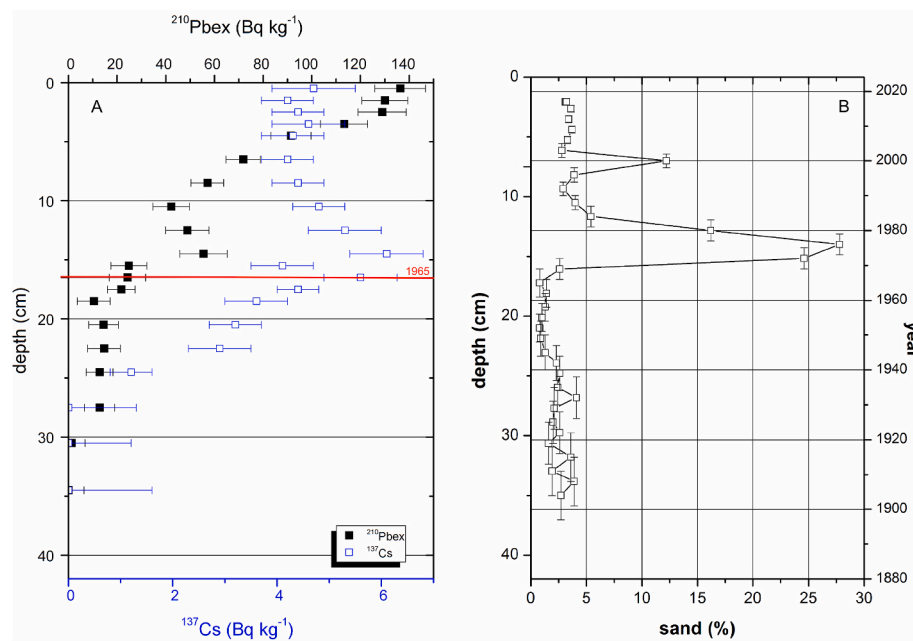


Fig. 5. A) Depth profiles of $^{210}\text{Pbex}$ and ^{137}Cs activities (Bq kg^{-1}) normalized to the pelitic fraction through the KR3 core; B) Depth profile of sandy fraction through the KR3 core.

^{137}Cs profile that marks 1963 (Buffoni et al., 2020) has been observed in the layer 16–17 cm (age 1965 ± 4 ; Fig. 5A).

We have also applied the CRS dating model, but the “knee” age in ^{137}Cs activity profile results 1957 ± 2 , without matching 1963. Only for CFCs dating model, ^{137}Cs profile confirms the ^{210}Pb dating. The ^{226}Ra and ^{40}K specific activities range around $26 \pm 2 \text{ Bq kg}^{-1}$ and $720 \pm 20 \text{ Bq kg}^{-1}$, respectively.

In the KR13, the age has been determined using the CRS (Constant Rate of Supply) dating model. The $^{210}\text{Pb}_{\text{ex}}$ dating has been similarly confirmed by the ^{137}Cs trend. Having applied the CRS model, no age can be estimated for layers deeper than the equilibrium depth (19 cm Fig. S7A). The ^{226}Ra specific activity ranges around $29 \pm 1 \text{ Bq kg}^{-1}$, similarly to KR3 core. Since the same values are observed in layers older than the industrial age, it is possible to consider $28 \pm 2 \text{ Bq kg}^{-1}$ as an average natural value in the area. The ^{40}K specific activity ranges around $720 \pm 30 \text{ Bq kg}^{-1}$ as the KR3 core.

4.3.2. Grain size and heavy metals

The grain size distribution in the two sediment cores KR3 and KR13 is dominated by silt (51–69%, and 55–58%, respectively) and clay (21–41% and 40–45%, respectively). The depth profile of sands in KR3 core (Fig. 5B) shows two peaks at 7–8 cm (with a maximum of 12%) and at 12–15 cm (with

a maximum of 28%), that correspond (on the basis of the achieved age model) to the year 2000 ± 2 and to a period between the years 1972 ± 5 and 1980 ± 5 , respectively (Fig. 5B). KR13, in contrast does not show evidence of specific trends with depth (Fig. S7).

To mitigate the effects due to the grain size differences caused by the presence of rich-sand levels and to clearly evidence the increase of Zn, Pb and Cu contents related to the effects of contamination, we have normalized the metals concentration values to the finer grain size fraction (silt + clay). In the KR3 core from the bottom to the top, the Zn_{norm} exhibits an increasing trend with the highest values ($\text{Zn}_{\text{norm}} > 1.2$) in the interval 13–21 cm, reflecting the extra-supply of Zn during the period of

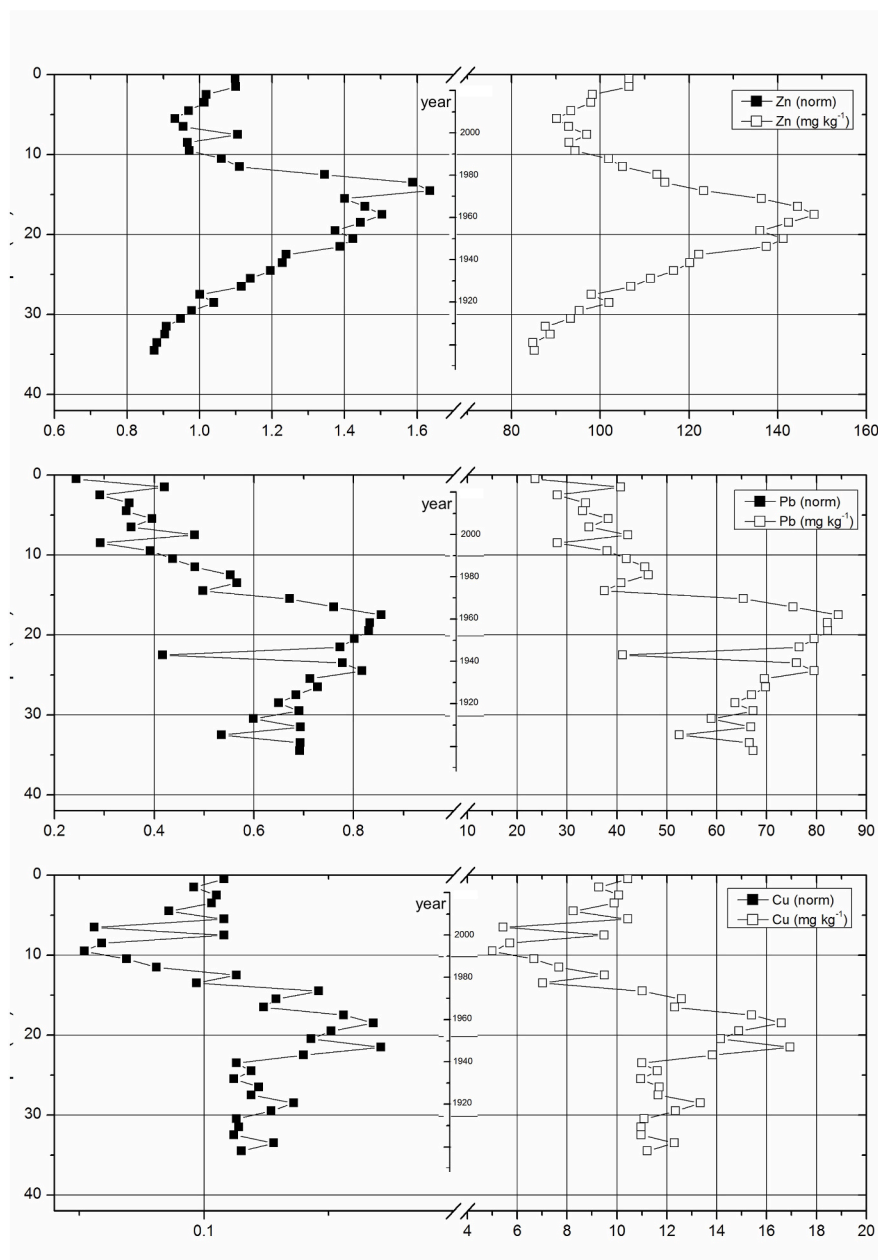


Fig. 6. Profiles of Cu, Pb, Zn normalized to finer fraction (silt + clay) and as total concentrations through the KR3 sediment core.

maximum industrial activity between 1949 and 1976 (Fig. 6). The relatively lower Zn_{norm} values in the interval 10–13 cm (1975–1980) suggests a temporal reduction of Zn industrial production as reported by Sorrentino (2018). Finally, the lowest Zn background values ($Zn_{norm} < 1$) below 28 cm (1904–1925) clearly document a time interval of pre-industrial activity (Fig. 6). The sharp peaks of Zn documented at 7–8 cm ($Zn_{norm} = 1.1$) and 12–15 cm ($Zn_{norm} = 1.6$) coincide with the two peaks of sandy material and suggest input of coarse-grained sediment with elevated Zn concentrations (Fig. 6). Similar increasing trend in the interval 13–21 cm has been documented for Pb_{norm} and Cu_{norm} , and coincides with the greater industrial activity (Fig. 6). However, high values of Pb and Cu in the lower interval of the core could reasonably document effects of historical mining activities present in the area (Larocca and Breglia, 2016).

In the core KR13, from the bottom to the top, the Zn_{norm} shows a relative increase of values ($Zn_{norm} > 1$) in the uppermost sediments which, following the age model, records the chronological evolution of industrial activity in the interval 12–13 cm (1940; Fig. S8). Analogue trends emerge for Pb_{norm} and Cu_{norm} with higher values above the interval 12–13 cm (Fig. S8). However, the Pb_{norm} concentrations show a sudden increase at the interval 20 cm (Fig. S7).

4.4. Naturally Occurring Radioactive Materials (NORM)

NORM measurements on the surficial sediments (0–5 cm) in the offshore sector are reported in Fig. 7. The yellow sandy samples (black circle; Fig. 7) show lower ^{226}Ra (average 8 Bq kg⁻¹) and higher ^{40}K activities (average 900 Bq kg⁻¹) with respect to the natural background documented by dated pre-industrial levels from the cores KR3 and KR13 (28 ± 2 Bq kg⁻¹ for ^{226}Ra ; 720 ± 30 Bq kg⁻¹ for ^{40}K ; red cross in Fig. 7). Differently, the ^{226}Ra and ^{40}K activities in the dark grey sands (blue circle; Fig. 7) result to be in good agreement with the average natural background. It is worth to note that the three records P4, P3 and 10 document ^{226}Ra values significantly higher than the other records again emphasizing hot spots of anthropogenic input (green circle; Fig. 7).

5. Discussion

5.1. Mechanisms of land-to-sea sediment transfer

According to the streamlines derived by the DTM analysis (Fig. 8A), an overall eastward coastline sediment supply may be reasonably forced by the slope changes and morphologic boundaries that essentially controls the sediment delivery from land. Differently, the lower slope values on the shelf (<0.5° down to -20 m b.s.l. and ~1° down to -70 m b.s.l., Fig. 8A) reduce the importance of the gravity-driven transport with

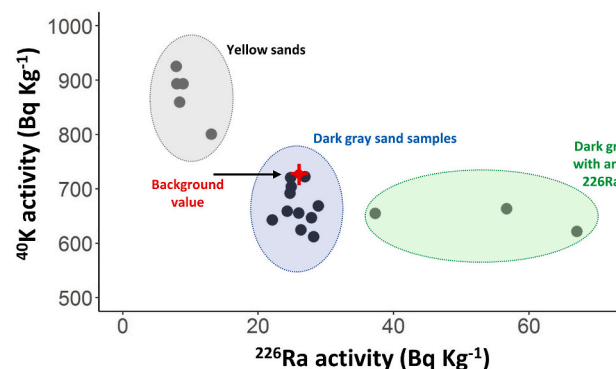


Fig. 7. Plot of ^{226}Ra and ^{40}K activities measured in superficial sediments. Blue circle: dark grey sand samples; Red cross: background value; Black circle: yellow sands; Green circle: dark grey sands with anomalous ^{226}Ra values. (For interpretation of the references to color in this figure legend, the reader is referred to the Web version of this article.)

respect to oceanographic factors such as wave regimes, marine currents, etc. (Flemming, 1981). Indeed, Iwasaki and Parker (2020) emphasized that these oceanographic factors may potentially be co-responsible, together with the sea-level changes, of the shelf emplacement. The Al distribution in surface sediments reveals a N–S onshore-to-offshore mechanism of sediment transport characterized by a limited oceanographic-driven mixing (Fig. 8A). In particular, a general eastward sediment transport can be inferred as the result of gravity-driven sediment supply that preserves the original difference in mineralogical and compositional contents from Neto and Esaro Rivers. The contribution from the Esaro River seems to be well-supported by evidence of increasing supply of clay minerals and calcite to sediments (Fig. 2B), reasonably fueling the marine deposits by the argillaceous rocks of the Argilla di Cutrò formation and the carbonate marine terraces characterizing the Plio-Quaternary Esaro drainage system (Zecchin et al., 2012, 2020; Roda, 1964; Fig. 1B). Differently, the quartz-felspathic composition of sediments from the northern sector (Fig. 2B) seems to well-reflect lithogenic fractions influenced by detrital inputs from the peri-Ionian land system (mainly Sila Massif) through Neto River (Perri et al., 2012).

In addition, the estuarine morphology revealed by both the Passovecchio (Fig. 8B) and Esaro (Fig. 8C) river mouths suggests a relatively low-energy (in correspondences of the barriers) and low-sediment supply settings. In particular, the Esaro estuarine morphology shows sediment features which reflect transgression events of marine water inside the river mouth (Fig. 8C). Shoreward of the breaking zone by wave-induced cross-shore sediment and longshore sediment transport emplaced the Passovecchio Estuarine (as it happens at a very large scale on the Senegal River Delta; Barusseau et al., 1998). The resulting Passovecchio Estuarine morphology, as well as the onset of across-track barriers and spits (FitzGerald et al., 2015; Fig. 2C) at the Esaro clearly indicate wave-dominated estuarine systems and an overall scarcity of sediment supply.

All this suggests that most of the recent sediment supply on the shelf originates from flash floods from land and successive eastward transport delivered to the Esaro and Neto-Lipuda Canyons (Fig. 8A–C).

5.2. Dispersion of contaminants from the coastal system to the offshore

The spatial distribution of heavy metals suggests a significant contamination of sediments in the “impact area” (Fig. 3). The Zn maps clearly show plumes of contamination located in the areas next to the Esaro river mouth where major transport of pollutants from land occurred during floods. The “external area” seems to be substantially unaffected by a direct contamination, except for the area identified by the three DTS09 cores (S105, S109, S112; Fig. S9) and the DTS17 box-cores (29, 17, 16; Fig. 4) where the Zn concentrations are significantly higher than the background level (Tab. S4). In all those cases (except for S109) the increase of Zn concentrations is accompanied by an increase of finer-grained fractions (silt + clay) that seems to indicate a major input from Esaro River. In addition, the mineralogical data evidence an important increase of calcite and clay minerals in the Zn-enrich layers of DTS17 samples supporting again an important input from the Esaro River (Fig. 2B). This evidence suggests that the deposition of those Zn-enrich layers resulted by impulsive transfers of contaminated sediments from the “impact area” to the offshore zone connected to flash flood events of the Esaro River. The hydrogeological instability reported for the study area is well recorded by the number of floods documented in the last century. Indeed, Canale et al. (2020) have recognized in the Crotona area a concomitant occurrence of 17 floods and sea storms events from 1990 to 2017 with connected damages to buildings and infrastructures. The flood event of 1996, triggered by the overflow of the Esaro River, was historically documented by significant damage of infrastructure in all the urbanized areas, including the harbor area (Macchione et al., 2019; Costabile et al., 2020). This flood generated a massive transport of sediments from land to the sea and a relevant mobilization of highly polluted material from the “impact area” to the

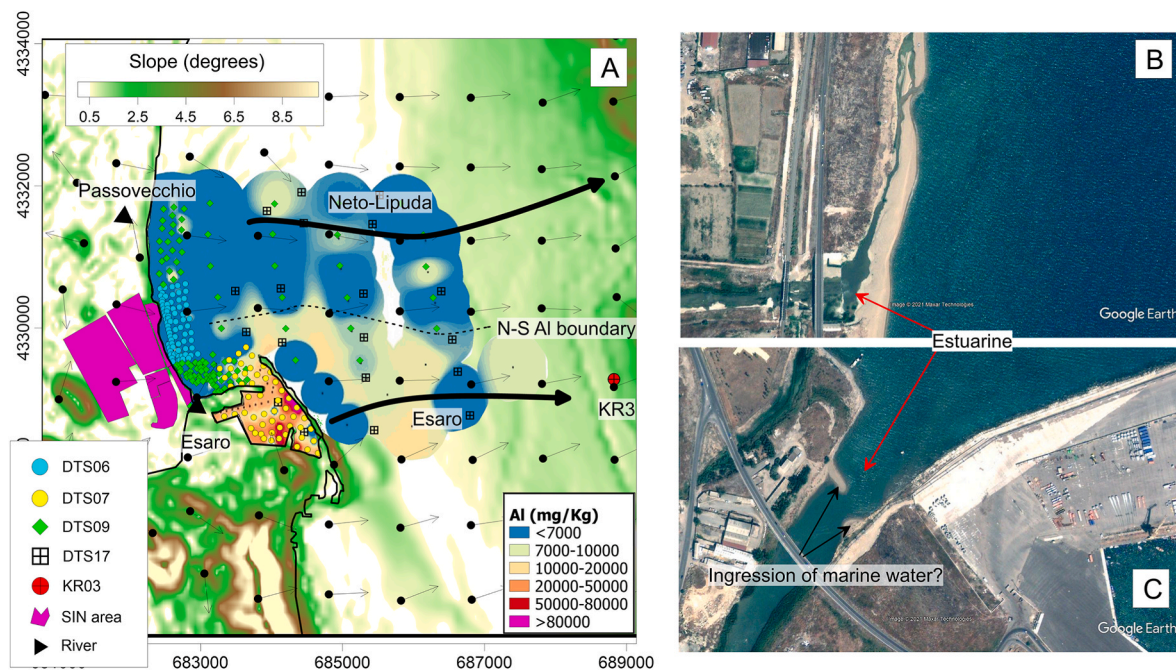


Fig. 8. Distribution map of Al on the Croton shelf (color map) and vectors showing principal streamlines. Vectors have been calculated as slope directions from the DTM. B) The Passovecchio stream mouth. C) The Esaro River mouth. B and C were obtained by google earth imagery (<https://www.google.it/intl/it/earth/>). (For interpretation of the references to color in this figure legend, the reader is referred to the Web version of this article.)

offshore. The same mechanism can be recognized in the offshore core KR3 which reliably documents the lithogenic inputs from the Esaro River and connected transport of industrial contaminants (Fig. 6). Particularly, the Zn peaks recorded at 7–8 cm ($Zn_{norm} = 1.1$) and 12–15 cm ($Zn_{norm} = 1.6$) document a high-energy coast-to-offshore mass transport reasonably linked to the major flood events of 1976 period and to the event of 1996. These peaks are linked to inputs of coarse-grained sediments (due to flood events) with 20–40% of finer grain size fraction that, presumably, with their very high values of Zn concentrations, document, in terms of bulk mass balance, peaks along the sediment profile.

The KR13 core does not show a detailed sequence of those events, although a weak rise of values ($Zn_{norm} > 1$) in the uppermost sediments testify the industrial temporal interval (Fig. S8). Re-distribution of the polluted sediments from the impact area to the offshore system testifies the effects of flood events on sediment dynamics. Most of this secondary pollution seems to principally affect areas along a W-E trajectory (29, 17, 16, KR3, Fig. 1D; S105, S109, S112; Fig. 3) following the main streamline of the Esaro River that plays a critical role in the resuspension/redeposition dynamics of this coastal environment. Also, the Esaro canyon act as a natural channel for pollutants from the shelf to the deep sea, potentially amplifying the effects of contamination to a wider marine area.

The documented high-sensitivity of the offshore marine system to natural risks on the coastal area, represents a crucial aspect to consider for appropriate and sustainable territory management. The strong interconnection between land and sea and the delicate deep-sea ecosystem demand comprehensive understanding of the dynamics involving anthropogenic contamination and natural risk assessment. A multi-hazard approach and inclusive modelling systems are required for a modern management of areas characterized by high-anthropogenic pressure.

Also, scenarios of climate change reported by the IPCC documents (IPCC, 2017) indicate an increasing trend, in frequency and intensity of impulsive flooding triggered by powerful runoff, mainly in the southern part of the central Mediterranean Sea and compel specific consideration of the documented cumulative effects of natural and anthropic impacts.

5.3. Recent industrial sands

A peculiar mineralogical feature characterizes the sediments of the 29, 16, 17, and 30 cores (Fig. S1). Indeed, in these sedimentary records, the topmost 5–10 cm are characterized by a thick layer of yellow sand (95–100%), superimposed on silty sediments. The mineralogical association is characterized by high percentages of K-feldspar (Fig. 2B) and allow us to classify these yellow sands as arkosic arenite (Folk, 1968). Additional mineralogical information by SEM analysis revealed traces of Ca-rich silicates with Si/Al which are atypical for natural feldspar. These Ca-silicates are firstly documented as zeolite or synthetic silicates because of their high Ca contents ($Ca/Si > 1$) and minor contents of Fe and Mg (Villa et al., 2010). Likewise, the measured high Ca/Si ratios could be associated to artificial silicates from industrial treatment of K-feldspar (Liu et al., 2019). Remarkably, the NORM distribution confirms a non-natural origin of this material with ^{226}Ra (average 8 Bq kg^{-1}), ^{40}K (average 900 Bq kg^{-1}) significantly different from those measured in natural background (29 Bq kg^{-1} for ^{226}Ra ; 700 Bq kg^{-1} for ^{40}K) (Fig. 7). Similar values of radioactivity have been measured in aggregates of building material ($^{226}Ra = 4–69$ Bq kg^{-1} ; $^{40}K = 22–964$ Bq kg^{-1} ; Trevisi et al., 2018) and in tile manufacture ($^{226}Ra = 20–90$ Bq kg^{-1} ; $^{40}K = 500–1000$ Bq kg^{-1} , Bruzzi et al., 1991).

The combination of these mineralogical and chemical (and radio-chemical) features seems to suggest an industrial origin for the yellow sands, associated with the production of tile manufacture which operated since 2003 and the zeolite production previously active in the same industrial plant (termed Gres-2000 after Sasol). Also, the industrial sands can contain abundant K-feldspars because of their ability as fluxing agent in the production cycle of ceramics (Valchev et al., 2014; Joaquim and Pereira Junior, 2016; Silva et al., 2019). We reasonably suppose that the yellow sand layers in the southern sector (top of the core offshore 29, 17, 16, 30, 18) testify recent dumping of synthetic material produced by industrial processes active in the chemical plant on land.

6. Conclusion

The reported multi-proxy investigation of the sedimentary records from the Crotone's coastal system offered an unprecedented opportunity to explore and estimate the dynamics of contaminants discharged from historical industrial activities combined to the effects of extreme geological hazards. Indeed, precisely dated events of flooding triggered remobilization and transport offshore of huge amount of highly contaminated sediments deposited alongshore during periods of intensive industrial activities. Thus, a coastal to offshore connections appears crucial in controlling the real spatial scale of the contamination impact alongshore. Consequently, methodological approaches for appropriate risk reduction, such as remediation measure or to constrain of polluted sediments dispersion, are urgently requested to protect and preserve delicate deeper sea ecosystems, connected by deep morphology to the coasts. Highly polluted landfills and/or coastal dumpsites, where major anthropogenic contamination has resulted from intensive industrial activities, solicit a major effort and specific consideration, also in terms of integrated tools, for appropriate evaluation of multi-hazards associated to natural events impacting on the biogeochemical dynamics and spreading pollutants in the marine environment on highly variable temporal and spatial scales.

CRediT authorship contribution statement

Elvira Oliveri: Writing – review & editing, Writing – original draft, Visualization, Methodology, Investigation, Conceptualization. **Antonella Ausili:** Writing – review & editing, Writing – original draft. **Mattia Barsanti:** Methodology, Investigation. **Fabio Conte:** Methodology, Investigation. **Ivana Delbono:** Writing – review & editing, Writing – original draft, Methodology. **Marianna Del Core:** Validation, Resources, Methodology. **Luigi Giaramita:** Resources. **Salvatore Passaro:** Writing – review & editing, Writing – original draft, Visualization, Software. **Francesco Placenti:** Resources. **Enza Maria Quinci:** Visualization, Formal analysis. **Elena Romano:** Writing – review & editing, Writing – original draft, Methodology. **Nadia Sabatino:** Writing – review & editing. **Antonio Schirone:** Writing – review & editing, Writing – original draft, Investigation, Formal analysis. **Giorgio Tranchida:** Resources. **Mario Sprovieri:** Writing – review & editing, Writing – original draft, Funding acquisition, Conceptualization.

Declaration of competing interest

The authors declare that they have no known competing financial interests or personal relationships that could have appeared to influence the work reported in this paper.

Acknowledgements

This work was supported by the CISAS project, a multidisciplinary project on environment/health relationships funded by the Italian Ministry of Education, Universities and Research (MIUR) and approved by the Interministerial Committee for Economic Planning (CIPE). The authors wish to thank the crew of R/V *MinervaUno* for their valuable professionalism and support to oceanographic cruise. We are grateful to Dr. V. Tancredi (IAS-CNR, Capo Granitola) and Dr V. Di Stefano (IAS-CNR, Capo Granitola) for their laboratory assistance. Thank are also due to the personnel of the port authorities of Crotone town and Dr. F. Bulfamante (IAS-CNR, Capo Granitola) for their precious logistic support for the research activities realized in the field.

Appendix A. Supplementary data

Supplementary data to this article can be found online at <https://doi.org/10.1016/j.ecss.2022.107854>.

References

- Alfieri, L., Bisselink, B., Dottori, F., Naumann, G., de Roo, A., Salamon, P., Wyser, K., Feyen, L., 2017. Global projections of river flood risk in a warmer world. *Earth's Future* 5, 171–182. <https://doi.org/10.1002/2016EF000485>.
- Appleby, P.G., Oldfield, F., 1983. The assessment of ^{210}Pb data from sites with varying sediment accumulation rates. *Hydrobiologia* 103, 29–35. <https://doi.org/10.1007/BF00028424>.
- Appleby, P.G., Oldfield, F., 1978. The calculation of lead-210 dates assuming a constant rate of supply of unsupported ^{210}Pb to the sediment. *Catena* 5, 1–8. [https://doi.org/10.1016/S0341-8162\(78\)80002-2](https://doi.org/10.1016/S0341-8162(78)80002-2).
- Arnell, N.W., Gosling, S.N., 2016. The impacts of climate change on river flood risk at the global scale. *Clim. Change* 134, 387–401. <https://doi.org/10.1007/s10584-014-1084-5>.
- Ausili, A., Bergamin, L., Romano, E., 2020. Environmental status of Italian coastal marine areas affected by long history of contamination. *Front. Environ. Sci.* 8, 34. <https://doi.org/10.3389/fenvs.2020.0003>.
- Barahona, E., Huertas, F., Pozzuoli, A., Linares, J., 1982. Mineralogia e genesi dei sedimenti della provincia di Granada (Spagna). *Acta Minerol.-Petrogr. (Szeged)* 26, 61–90.
- Barousseau, J.-P., Ba, M., Descamps, C., Diop, E.H.S., Kane, A., Saos, J.-L., et Soumar, A., 1998. Morphological and sedimentological changes in the estuary Senegal river after the construction of the Diama dam. *J. Afr. Earth Sci.* 26, 317–326. [https://doi.org/10.1016/S0899-5362\(98\)00014-1](https://doi.org/10.1016/S0899-5362(98)00014-1).
- Bonardi, G., Cavazza, W., Perrone, V., Rossi, S., 2001. Calabria-peloritani terrane and northern Ionian Sea. In: Vai, G.B., Martini, I.P. (Eds.), *Anatomy of an Orogen: the Apennines and Adjacent Mediterranean Basins*. Springer, Dordrecht, pp. 287–306. https://doi.org/10.1007/978-94-015-9829-3_17.
- Bonsignore, M., Salvaggio Manta, D., Oliveri, E., Sprovieri, M., Basile, G., Bonanno, A., Falco, F., Traina, A., Mazzola, S., 2013. Mercury in fishes from Augusta Bay (southern Italy): risk assessment and health implication. *Food Chem. Toxicol.* 56, 184–194. <https://doi.org/10.1016/j.fct.2013.02.025>.
- Borch, T., Kretzschmar, R., Kappler, A., Van Capellen, P., Ginder-Vogel, M., Voegelin, A., Campbell, K., 2010. Biogeochemical redox processes and their impact on contaminant dynamics. *Environ. Sci. Technol.* 44, 5–23. <https://doi.org/10.1021/es9026248>.
- Bradley, P.M., Journey, C.A., Chapelle, F.H., Lowery, M.A., Conrads, P.A., 2010. Flood hydrology and methylmercury availability in coastal plain rivers. *Environ. Sci. Technol.* 44, 9285–9290. <https://doi.org/10.1021/es102917j>.
- Bruzzi, L., Cazzoli, S., Mele, R., Tenaglia, A., 1991. Natural radioactivity in ceramic products for the building industry: ceramic floor and wall tile. *Ceramica Acta* 3, 27–36.
- Buffoni, G., Schirone, A., Delfanti, R., 2020. A numerical investigation for dating ^{210}Pb and ^{137}Cs vertical profiles in a coastal area: the Eastern Ligurian Sea, Italy. *J. Environ. Radioact.* 212, 106–122. <https://doi.org/10.1016/j.jenvrad.2019.106122>.
- Canale, C., Barbaro, G., Petrucci, O., Besio, G., Foti, G., Barilla, G.B., Puntorieri, P., 2020. Analysis of the concurrent conditions of floods and sea storms: a case study of Crotone, Italy. In: Syngellakis, S., Fabbri, A. (Eds.), *Risk Analysis XII*, WIT Transaction on Engineering Sciences, 129. WIT Press, pp. 147–156. <https://doi.org/10.2495/RISK200131>.
- Conforto, P., Plank, S., Di Martire, D., Ramondini, M., Thuro, K., Calcaterra, D., 2015. Slow-moving landslide monitoring with multi-temporal terra SAR-X data by means of DInSAR techniques in Crotone province (southern Italy). In: Ouwehand, L. (Ed.), *FRINGE 2015, Proceedings of the Workshop Held 23-27 March, 2015 in Frascati*, 731. Italy. ESA-SP id.23.
- Costabile, P., Costanzo, C., De Lorenzo, G., Maccione, F., 2020. Is local flood hazard assessment in urban areas significantly influenced by the physical complexity of the hydrodynamic inundation model? *J. Hydrol.* 580, 124231. <https://doi.org/10.1016/j.jhydrol.2019.124231>.
- Currie, L.A., 1968. Limits for qualitative detection and quantitative determination. Application to radiochemistry. *Anal. Chem.* 40 (3), 586–593. <https://doi.org/10.1021/ac60259a007>.
- Cutshall, N.H., Larsen, I.L., Olsen, C.R., 1983. Direct analysis of ^{210}Pb in sediment samples: self-absorption corrections. *Nucl. Instrum. Methods: Phys. Res.* 206 (1–2), 309–312.
- Ferranti, L., Santoro, E., Mazzella, M.E., Monaco, C., Morelli, D., 2009. Active transpression in the northern Calabria Apennines, southern Italy. *Tectonophysics* 476, 226–251. <https://doi.org/10.1016/j.tecto.2008.11.010>.
- FitzGerald, D., Georgiou, I., Miner, M., 2015. Estuaries and tidal inlets. In: Masselink, Gerd, Gehrels, Roland (Eds.), *Coastal Environments and Global Change*. John Wiley & Sons, Ltd. <https://doi.org/10.1002/978111917261>.
- Flemming, B.W., 1981. Factors controlling shelf sediment dispersal along the southeast African continental margin. *Mar. Geol.* 42 (1–2), 259–277. [https://doi.org/10.1016/0025-3227\(81\)90166-3](https://doi.org/10.1016/0025-3227(81)90166-3).
- Folk, R.L., 1968. *Petrology of Sedimentary Rock*. Hemphill's, Austin, Texas, p. 170.
- IAEA 599 (INTERNATIONAL ATOMIC ENERGY AGENCY VIENNA), 2013. Radiation protection and management of NORM residues in the phosphate industry. ISSN 1020-6450 Safety Rep. Series (78). ISBN 978-92-0-135810-3.
- Intergovernmental Panel on Climate Change, 2017. *IPCC Fifth Assessment Report (AR5) Observed 753 Climate Change Impacts Database, Version 2.01*. NASA Socioeconomic Data and Applications 754 Center (SEDAC). Palisades, NY.
- Irabien, M.J., Cearreta, A., Gómez-Arozamena, J., Serrano, H., Sanchez-Cabeza, J.-A., Ruiz-Fernández, A.C., 2019. Geological record of extreme floods and anthropogenic impacts on an industrialised bay: the inner Abra of Bilbao (northern Spain). *Sci. Total Environ.* 696, 133946. <https://doi.org/10.1016/j.scitotenv.2019.133946>.

- Iwasaki, T., Parker, G., 2020. The role of saltwater and waves in continental shelf formation with seaward migrating clinoform. *Proc. Natl. Acad. Sci. Unit. States Am.* 117 (3), 1266–1273. <https://doi.org/10.1073/pnas.1909572117>.
- Joaquim, L.G., Pereira Júnior, R.F., 2016. Feldspato. In: Lima, T.M., Neves, C.A.R. (Eds.), *Sumário Mineral 2015*. DNPM, Brasília, pp. 64–65.
- Kowalewska, G., Belzunce-Segarra, M.J., Schubert, B., Heininger, P., Heise, S., 2011. The role of sediments in coastal monitoring. In: Quevauviller, P., Roose, P., Verreert, G. (Eds.), *Chemical Marine Monitoring: Policy Framework and Analytical Trends*. John Wiley & Sons, Hoboken, NJ, pp. 377–395. <https://doi.org/10.1002/9781119990826.ch12>.
- Krishnaswamy, S., Lal, D., Martin, J.M., Meybeck, M., 1971. Geochronology of lake sediments. *Earth Planet Sci. Lett.* 11, 407–414. [https://doi.org/10.1016/0012-821X\(71\)90202-0](https://doi.org/10.1016/0012-821X(71)90202-0).
- Larocca, F., Breglia, F., 2016. Grooved stone tools from Calabria region (Italy): archaeological evidence and research perspectives. *J. Lithic Stud.* 3 (3), 301–312. <https://doi.org/10.2218/jls.v3i3.1673>.
- Le Pera, E., Critelli, S., Sorriso-Valvo, M., 2001. Weathering of gneiss in Calabria, southern Italy. *Catena* 42 (1), 1–15. [https://doi.org/10.1016/S0341-8162\(00\)00117-X](https://doi.org/10.1016/S0341-8162(00)00117-X).
- Liu, S., Han, C., Liu, J., 2019. Study of K-feldspar and lime hydrothermal reaction: phase and mechanism with reaction temperature and increasing Ca/Si ratio. *Minerals* 9 (1), 46. <https://doi.org/10.3390/min9010046>.
- Macchione, F., Costabile, P., Costanzo, C., De Lorenzo, G., 2019. Extracting quantitative data from non-conventional information for the hydraulic reconstruction of past urban flood events. A case study. *J. Hydrol.* 576, 443–465. <https://doi.org/10.1016/j.jhydrol.2019.06.031>.
- Marín-Guirao, L., Lloret, J., Marín, A., García, G., García-Fernández, A.J., 2007. Pulse-discharges of mining wastes into a coastal lagoon: water chemistry and toxicity. *Chem. Ecol.* 23, 217–231. <https://doi.org/10.1080/02757540701339422>.
- Martínez-Santos, M., Probst, A., García-García, J., Ruiz-Romera, E., 2015. Influence of anthropogenic inputs and high-magnitude flood event on metal contamination pattern in surface bottom from the Deba River urban catchment. *Sci. Total Environ.* 514, 10–25. <https://doi.org/10.1016/j.scitotenv.2015.01.078>.
- Massari, F., Prosser, G., Capraro, L., Fornaciari, E., Consolaro, C., 2010. A revision of the stratigraphy and geology of the south-western part of the Crotona Basin (South Italy). *Bollettino Società Geologica Italiana* 129 (3), 353–384.
- Massarra, C.C., Friedland, C.J., Marx, B.D., Dietrich, J.C., 2019. Predictive multi-hazard hurricane data-based fragility model for residential homes. *Coast. Eng.* 151, 10–21. <https://doi.org/10.1016/j.coastaleng.2019.04.008>.
- Mendicino, G., 2006. Rainfall and hydrometric thresholds for flood warning. The Esaro river case study. In: Ferrari, E., Versace, P. (Eds.), *Observing and Modelling Exceptional Floods and Rainfalls*, Proceedings of the AMHY-FRIEND International Workshop on Hydrological Extremes. held at University of Calabria, Cosenza (Italy), pp. 213–228. May 3–4.
- Messina, A., Compagnoni, R., De Vivo, B., Perrone, V., Russo, S., Barbieri, M., Scott, B., 1991. Geological and petrochemical study of the Sila Massif plutonic rocks northern Calabria, Italy. *Bollettino Società Geologica Italiana* 110, 165–206.
- Mitášová, H., Mitáš, L., 1993. Interpolation by regularized spline with tension: I. Theory and implementation. *Math. Geol.* 25, 641–655. <https://doi.org/10.1007/bf008993171>.
- Monhemius, J., 1980. The electrolytic production of zinc. In: Burkin, A.R. (Ed.), *Topics in Non-ferrous Extractive Metallurgy*, (Crit. Rep. Appl. Chem., 1. Blackwell Scientific Publications, Oxford, pp. 104–130.
- Ollivon, D., Blanchard, M., Garban, B., 1999. PAH fluctuations in rivers in the Paris region (France): impact of floods and rainy events. *Water, Air, Soil Pollut.* 115, 429–444. <https://doi.org/10.1023/A:1005162128490>.
- Oursel, B., Garnier, C., Zebracki, M., Durrieu, G., Pairaud, I., Omanović, D., Cossa, D., Lucas, Y., 2014. Flood inputs in a Mediterranean coastal zone impacted by a large urban area: dynamic and fate of trace metals. *Mar. Chem.* 167, 44–56. <https://doi.org/10.1016/j.marchem.2014.08.005>.
- Perri, F., Critelli, S., Dominici, R., Muto, F., Tripodi, V., Ceramicola, S., 2012. Provenance and accommodation pathways of late Quaternary sediments in the deep-water northern Ionian Basin. *Southern Italy Sedimentary Geol.* 280, 244–259. <https://doi.org/10.1016/j.sedgeo.2012.01.007>.
- Petrucchi, O., Chiodo, G., Caloiero, D., 1996. Eventi alluvionali in Calabria nel decennio 1971–1980. CNR-GNDICI (Consiglio Nazionale delle Ricerche-Gruppo Nazionale per la Difesa dalle Catastrofi Idrogeologiche), Pub. N. 1374. Rubbettino arti Grafiche, Soveria Mannelli (CZ), p. 142. <http://books.google.it/books?id=JqQtrXZhkpsC>.
- Petrucchi, O., Dodaro, S., 1998. Le alluvioni storiche nell'area del crotonese. In: Gabriele, S. (Ed.), *Crotone e l'evento alluvionale dell'ottobre 1996*. CNR-GNDICI (Consiglio Nazionale delle Ricerche-Gruppo Nazionale per la Difesa dalle Catastrofi Idrogeologiche), Pub. N. pp. 23–30, 1891.
- Petrucchi, O., Pasqua, A.A., Polemio, M., 2012. Flash flood occurrences since the 17th century in steep drainage basins in southern Italy. *Environ. Manag.* 50, 807–818. <https://doi.org/10.1007/s00267-012-9935-1>.
- Rebesco, M., Neagu, R.C., Cuppari, A., Muto, F., Accetella, A., Dominici, R., Coca, A., Romano, C., Caburlotto, A., 2009. Morphobathymetric analysis and evidence of submarine mass movements in the western Gulf of Taranto (Calabria margin, Ionian Sea). *Int. J. Earth Sci.* 98, 791. <https://doi.org/10.1007/s00531-009-0429-1>.
- Robbins, J.A., 1978. Geochemical and geophysical applications of radioactive lead isotopes. In: Nriagu, J.O. (Ed.), *Biochemistry of Lead*. Elsevier, Amsterdam, pp. 85–393.
- Roda, C., 1964. Distribuzione e facies dei sedimenti Neogenici nel Bacino Crotonese. *Geol. Rom.* 3, 319–366. <https://www.gruppocarneoliticokr.it/biblioteca/cesare-roda-distribuzione-e-facies-dei-sedimenti-neogenici-nel-bacino-crotonese-1964/>.
- Roussiez, V., Ludwig, W., Radakovitch, O., Probst, J.-L., Monaco, A., Charrière, B., Buscail, R., 2011. Fate of metals in coastal sediments of a Mediterranean flood-dominated system: an approach based on total and labile fractions. *Estuar. Coast Shelf Sci.* 92, 486–495. <https://doi.org/10.1016/j.eccs.2011.02.009>.
- Salvagio Manta, D., Bonsignore, M., Oliveri, E., Barra, M., Tranchida, G., Giaramita, L., Mazzola, S., Sprovieri, M., 2016. Fluxes and the mass balance of mercury in Augusta Bay (Sicily, southern Italy). *Estuarine. Coast Shelf Sci.* 181, 134–143. <https://doi.org/10.1016/j.eccs.2016.08.013>.
- Sanchez-Cabeza, J.A., Ruiz-Fernández, A.C., 2012. ^{210}Pb sediment radiochronology: an integrated formulation and classification of dating models. *Geochim. Cosmochim. Acta* 82, 183–200.
- Schultz, L.G., 1964. Quantitative interpretation of mineralogical composition from X-ray and chemical data for the Pierre Shale, 391-C. U. S. Geol. Surv. Prof. Pap. 1–31.
- Sicre, M.A., Fernandes, M.B., Pont, D., 2008. Poly-aromatic hydrocarbon (PAH) inputs from the Rhône River to the Mediterranean Sea in relation with the hydrological cycle: impact of floods. *Mar. Pollut. Bull.* 56, 1935–1942. <https://doi.org/10.1016/j.marpolbul.2008.07.015>.
- Silva, A.C., Carolina, S.D., Sousa, D.N., Silva, E.M.S., 2019. Feldspar production from dimension stone tailings for application in the ceramic industry. *J. Mater. Res. Technol.* 8 (1), 1–7. <https://doi.org/10.1016/j.jmrt.2018.02.011>.
- Smith, J.N., 2001. Why should we believe ^{210}Pb sediment geochronologies? *J. Environ. Radioact.* 55, 121–123.
- Sorrentino, A., 2018. *Compagni di viaggio. Storia e uomini della Montecatini di Crotone*. CSA Ed., p. 400. -10: 8893540711.
- The MerMex Group, 2011. Marine ecosystems' responses to climatic and anthropogenic forcing in the Mediterranean. *Prog. Oceanogr.* 91, 97–166. <https://doi.org/10.1016/j.pcean.2011.02.003>.
- Trevisi, R., Leonardi, F., Risica, S., Nuccetelli, C., 2018. Updated database on natural radioactivity in building materials in Europe. *J. Environ. Radioact.* 187, 90–105. <https://doi.org/10.1016/j.jenvrad.2018.01.024>.
- U.S. EPA, 2014. Method 6020B (SW-846): Inductively Coupled Plasma-Mass Spectrometry. Revision 2. Washington, DC.
- Valchev, A., Ignatova, T., Grigorova, I., Nishkov, I., 2014. Recovery of feldspar and silica sand from arkosic sandstones. In: GECAMIN (Ed.), *Proceedings of the XXVII IMPC*, pp. 1–13. October 20–24, Santiago, Chile (2014).
- Velasco, J., Lloret, J., Millán, A., Marín, A., Barahona, J., Abellán, P., Sánchez-Fernández, D., 2006. Nutrient and particulate inputs into the Mar Menor lagoon (SE Spain) from an intensive agricultural watershed. *Water, Air, Soil Pollut.* 176, 37–56. <https://doi.org/10.1007/s11270-006-2859-8>.
- Viers, J., Dupré, B., Gaillardet, J., 2009. Chemical composition of suspended sediments in world rivers: new insights from a new database. *Sci. Total Environ.* 407, 853–868. <https://doi.org/10.1016/j.scitotenv.2008.09.053>.
- Villa, C., Pecina, E.T., Torres, R., Gómez, L., 2010. Geopolymer synthesis using alkaline activation of natural zeolite. *Construct. Build. Mater.* 24 (11), 2084–2090. <https://doi.org/10.1016/j.conbuildmat.2010.04.052>.
- Winsemius, H.C., Aerts, J.C.J.H., Van Beek, L.P.H., Bierkens, M.F.P., Bouwman, A., Jongman, B., Kwadijk, J.C.J., Ligtoet, W., Lucas, P.L., Van Vuuren, D.P., Ward, P.J., 2016. Global drivers of future river flood risk. *Nat. Clim. Change* 6. <https://doi.org/10.1038/NCLIMATE2893>.
- Yang, Y., Min, Y., Lococo, J., Jun, Y.-S., 2014. Effects of Al/Si ordering on feldspar dissolution: Part I. Crystallographic control on the stoichiometry of dissolution reaction. *Geochim. Cosmochim. Acta* 126, 574–594. <https://doi.org/10.1016/j.gca.2013.10.047>.
- Zecchin, M., Caffau, M., 2020. Emergence of a submarine canyon, Crotona Basin, southern Italy. *Mar. Petrol. Geol.* 114, 104204. <https://doi.org/10.1016/j.marpetgeo.2019.104204>.
- Zecchin, M., Civile, D., Caffau, M., Critelli, S., Muto, F., Mangano, G., Ceramicola, S., 2020. Sedimentary evolution of the Neogene-Quaternary Crotona Basin (southern Italy) and relationships with large-scale tectonics: a sequence stratigraphic approach. *Mar. Petrol. Geol.* 117, 104381.
- Zecchin, M., Nalin, R., Roda, C., 2004. Raised Pleistocene marine terraces of the Crotona peninsula (Calabria, southern Italy): facies analysis and organization of their deposits. *Sediment. Geol.* 172, 165–185. <https://doi.org/10.1016/j.sedgeo.2004.08.003>.
- Zecchin, M., Accaino, F., Ceramicola, S., Civile, D., Critelli, S., Da Lio, C., Mangano, G., Prosser, G., Teatini, P., Tosi, L., 2018. The Crotona Megalandslide, southern Italy: architecture, timing and tectonic control. *Sci. Rep.* 8, 7778. <https://doi.org/10.1038/s41598-018-26266-y>.
- Zecchin, M., Caffau, M., Civile, D., Critelli, S., Di Stefano, A., Maniscalco, R., Muto, F., Sturiale, G., Roda, C., 2012. The Plio-Pleistocene evolution of the Crotona Basin (southern Italy): interplay between sedimentation, tectonics and eustasy in the frame of Calabrian Arc migration. *Earth Sci. Rev.* 115 (4), 273–303. <https://doi.org/10.1016/j.earscirev.2012.10.005>.